Supporting Information

Electrochemical injection Oxygen Vacancies in Layered $Ca_2Mn_3O_8$ for Boosting Zinc-Ion Storage

Lipeng Wang[1,2], Ziyi Cao[1,2], Peiyuan Zhuang[1], Jiaxin Li[3], Hang Chu[1], Zhuolin Ye[1,2], Dongxiao Xu[1,2], Hong Zhang[1,2] Jianfeng Shen*[1], Mingxin Ye*[1]

[1] Institute of Special Materials and Technology, Fudan University, Shanghai, 200433, P. R. China

[2] Department of Chemistry, Fudan University, Shanghai, 200438, China

[3] State Key Laboratory of Molecular Engineering of Polymers Department of Macromolecular Science, Fudan University, Shanghai, 200438, China

Corresponding Author: *jfshen@fudan.edu.cn, mxye@fudan.edu.cn.

Experimental Section

Material Characterization:

The compositions and microstructures were investigated via FESEM (Tescan MAIA3 XMH, 10 kV), XRD with Cu Kα-radiation (Bruker D8 ADVANCE, λ=0.15405 nm, Cu Kα radiation, 40 kV, 40 mA), TEM (JEOL JEM-2100 LaB_6), XPS (PHI 5000C&PHI5300, Mg, 250 W, 14 kV) at room temperature. X-ray photoelectron spectra were calibrated with a carbon peak at 284.8 eV as a reference, and all samples were Ar etched before characterization.[2] The evolution of the element contents of electrode in solution was detected by ICP-OES. The EPR characterization was analyzed in the X-band (9.45 GHz) with 1.0 G modulation amplitude and a magnetic field modulation of 100 kHz through the Bruker, A300-10-12 Bruker EPR spectrometer at 100K. The in situ differential electrochemical mass spectrometry (DEMS) analysis was employed to track the gases generated during charging. The cell was purged continuously with Ar gas, which flows through the headspace of cell. The evolved gases from electrode was carried by Ar and was traced. The cell potential was raised from open potential to 1.8 V with the current density of 50 mA g^{-1}, and the variation of the ion current for different m/z (mass per electron) monitored as a function of time.

Electrochemical calculation:

The detailed calculations about the specific energy density and power density of the aqueous $Ca_2Mn_3O_8$//Zn battery were given as follows:

The specific energy density of the aqueous $Ca_2Mn_3O_8$//Zn cell was calculated according to the Equation 1.

$$Espe = C \times V/m \quad \text{(Eq. S1)}$$

where E*spe* is specific energy density (Wh kg^{-1}); C is the discharge capacity (Ah); V is the average discharge voltage (V); m is the total mass (Kg) of cathode ($Ca_2Mn_3O_8$).

The specific power density of the aqueous $Ca_2Mn_3O_8$//Zn cell is calculated according to Equation 2.

$$Pspe = i \times V/m \quad \text{(Eq. S2)}$$

where *Pspe* is specific power density (W kg^{-1}); *i* is applied current (A); V is average discharge voltage (V); m is the total mass (Kg) of cathode ($Ca_2Mn_3O_8$).

The coulombic efficiency of O_d-CMO and KMO as shown in the Equation 3.

$$Coulombic\ efficiency = \frac{Discharge\ capacity}{Charge\ capacity} \quad \text{(Eq. S3)}$$

The Zn ions storage kinetics can be divided into two main type: capacity-controlled process and diffusion-controlled process. The charge storage kinetics can be calculated according the Equation 4:

$$i = av^b \quad \text{(Eq 4)}$$

where *i* is the peak current and *v* is the scan rate based on the CV curves, and the above equation can be transformed as

$$\log(i) = b\log(v) + \log(a) \quad \text{(Eq 5)}$$

The value of b can be obtained through line fitting between log(*i*) and log(*v*).

Once *b* approaches 0.5, the specific capacity is dominated by battery-type behavior.

When the value is close to 1.0, the semi-infinite linear diffusion process is mainly driven by pseudocapacitance.[46] The capacity contribution can analyzed through the use of the equation below:

$$i = k_1 v + k_2 v^{1/2} \quad \text{(Eq 6)}$$

Where i is the current based on the CV curves, and $k_1 v$, and $k_2 v^{1/2}$ represent capacitive and ionic diffusion contribution, respectively.

The electrochemical active surface area was determined by estimating the capacitive current associated with double-layer charging from the scan-rate dependence of cyclic voltammetry (CV). The linear trend was obtained by fitting the difference in current density between cathodic and anodic sweeps at a certain potential under the various scan rate. The double-layer capacitance (C_{dl}) is a half of fitting slope, which have linear relation with the electrochemical active surface. The value of C_{dl} is a powerful evidence to compare the relative surface activity of various electrodes. The potential window of CV curves was 1.42 V - 1.52 V vs. Zn^{2+}/Zn with the scan rate from 0.1 mV/s – 1.0 mV/s to measure the C_{dl} for different electrode.[3,4]

DFT Calculation:

In this work, all DFT calculations were performed in the Materials Studio (Accelrys) package by CASTEP code. The generalized gradient approximation in the form of Perdew–Burke–Ernzerhof functional was selected to estimate the electron exchange-correlation potential with the TS method for dispersion (DFT-D) corrections. A 2 × 2 × 1 k-point mesh was chosen based on the Monkhorst–Pack method with a 550

eV energy cutoff. The $Ca_2Mn_3O_8$ surface was cleaved to (200) plane with a vacuum of 10 Å. Geometry optimization was performed by using the Broyden–Fletcher–Goldfarb–Shanno method. The energy of 2.0×10^{-5} eV per atom, the maximum force of 0.05 eV per Å, and the maximum displacement of 0.002 Å were utilized as the conditions of convergence tolerance.

The binding energy of zinc atom adsorption (ΔG), which was the main parameter of evaluating the energy barrier of insertion, was calculated with the following equation:

$$\Delta G = G_{\text{cell+Zn}} - G_{\text{Zn}} - G_{\text{cell}} \quad \text{(Eq. S7)}$$

Where $G_{\text{cell+Zn}}$, G_{Zn} and G_{cell} were the total free energy of the different cell with absorbed Zn, a Zn atom in the solid phase and the used cell.

Results and Discussion

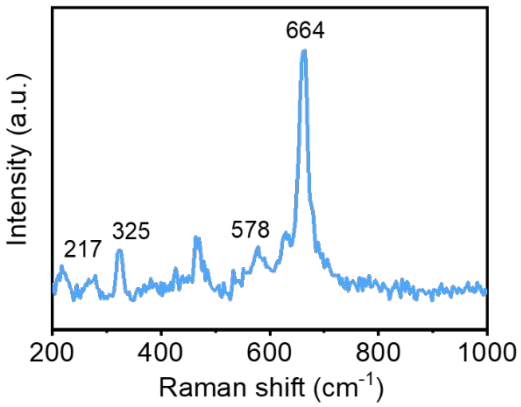

Figure S1. a) The Raman spectra of $Ca_2Mn_3O_8$.

The sharp characteristic peak at 664 cm^{-1} is assigned to the *v*2 (Mn-O) stretching vibration of the MnO_6 octahedron. Other small peaks at 578, 325 and 217 cm^{-1} are corelated to the *v*3 (Mn-O) stretching vibration, the Mn-O-Mn vibration and the Ca-O stretching vibration, respectively.[5,6]

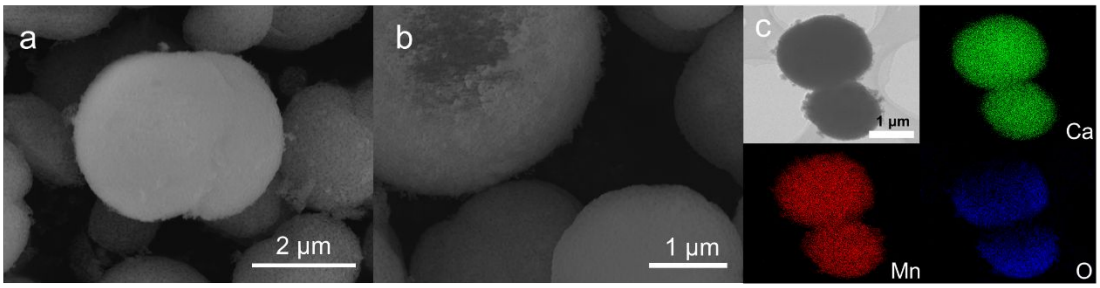

Figure S2. a), b) SEM images, and c) EDS element mapping of $Ca_2Mn_3O_8$.

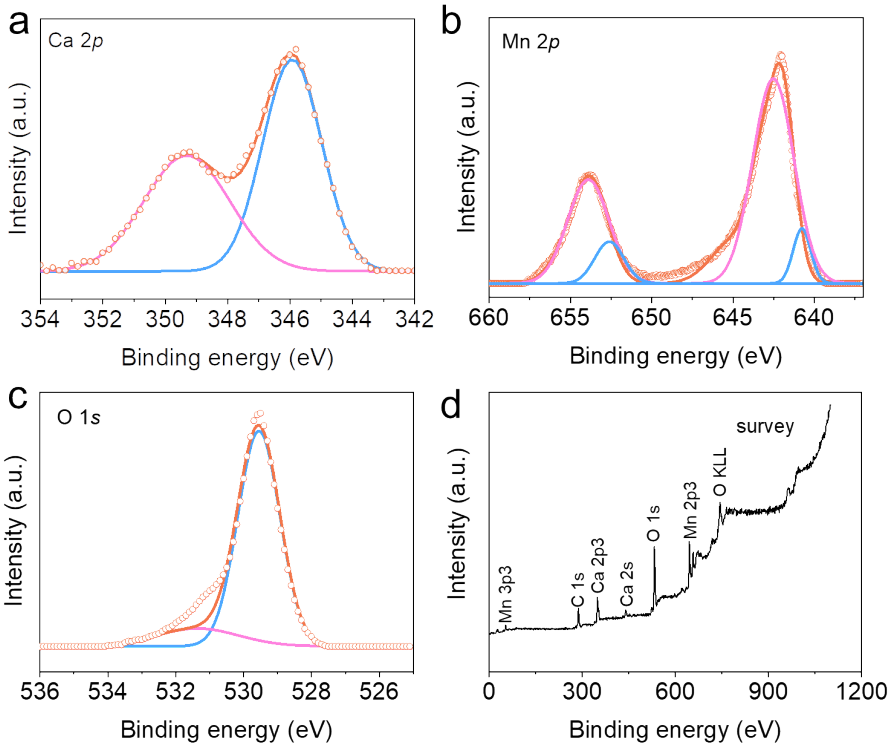

Figure S3. The high-resolution a) Ca 2p, b) Mn 2p, c) O 1s XPS spectra and d) XPS survey spectra of $Ca_2Mn_3O_8$.

The normalized Mn 2p spectrum (Figure S3b) reveals two characteristic peaks concerting to Mn $2p_{1/2}$ and Mn $2p_{3/2}$.[7] Based on the deconvoluted high-resolution O 1s spectrum (Figure S3a), the obvious peak situated at 531.2 and 529.0 eV and tiny peak located at 531.2 are attributed to lattice oxygen and defective oxygen, respectively.[8]

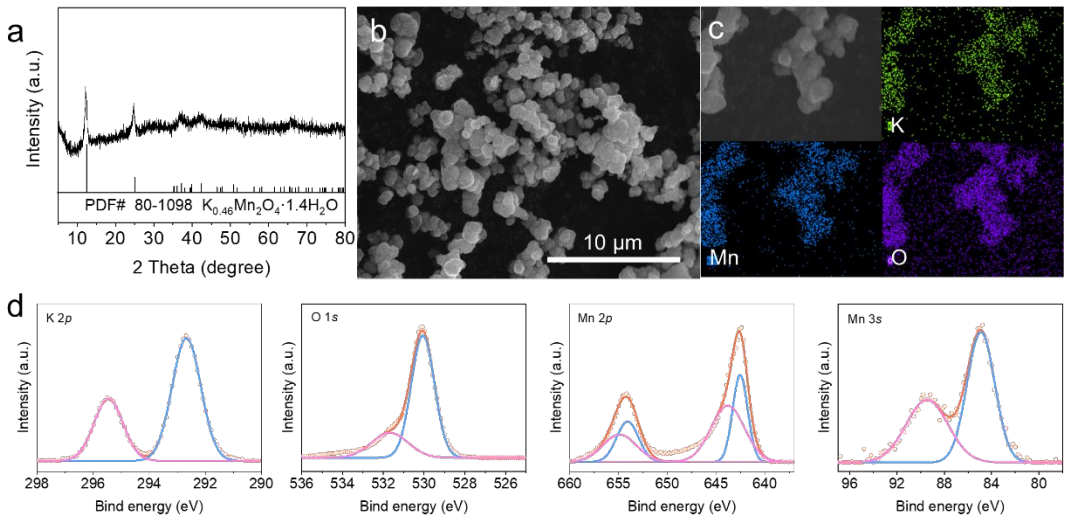

Figure S4. The characterization of a) XRD, b) SEM, c) EDS element mapping, and d) XPS spectra of δ- $K_{0.46}Mn_2O_4 \cdot 1.4H_2O$.

The XRD pattern (Figure S4a) reveals the layered structure of $K_{0.46}Mn_2O_4 \cdot 1.4H_2O$ with great crystallinity, indexing to the Birnessite (PDF# 80-1098). The SEM image (Figure S3b) show the nanoflowers morphology, coinciding with the previous work.[1] The EDS analysis (Figure S3c) demonstrate the uniform distribution of K, Mn and O elements, and the K comes from the hydrothermal residue of $KMnO_4$. The normalized Mn 2p spectrum (Figure S4d) reveals two characteristic peaks concerting to Mn $2p_{1/2}$ and Mn $2p_{3/2}$. The layered K ions cause the reduced valance of Mn.

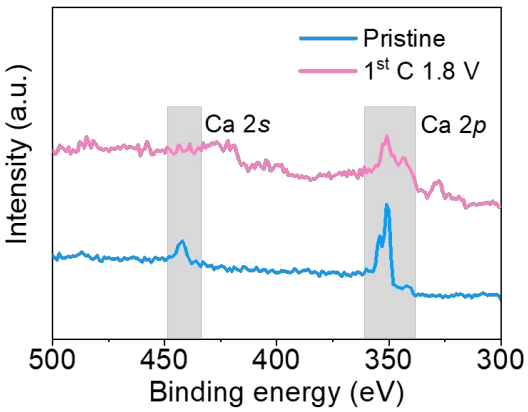

Figure S5. The XPS spectra of initial and fully charged electrode.

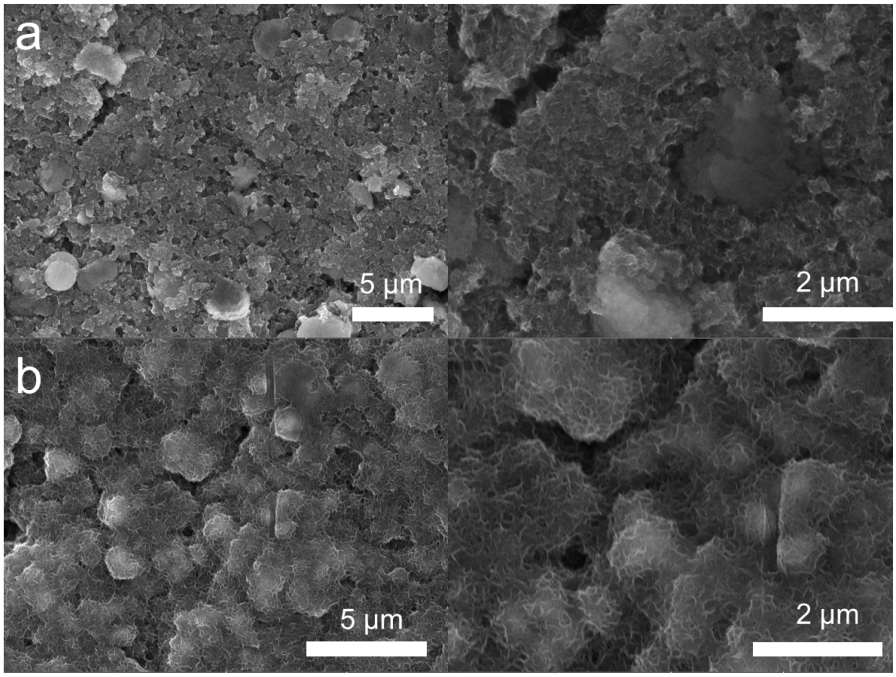

Figure S6. The SEM of a) initial and b) fully charged electrode.

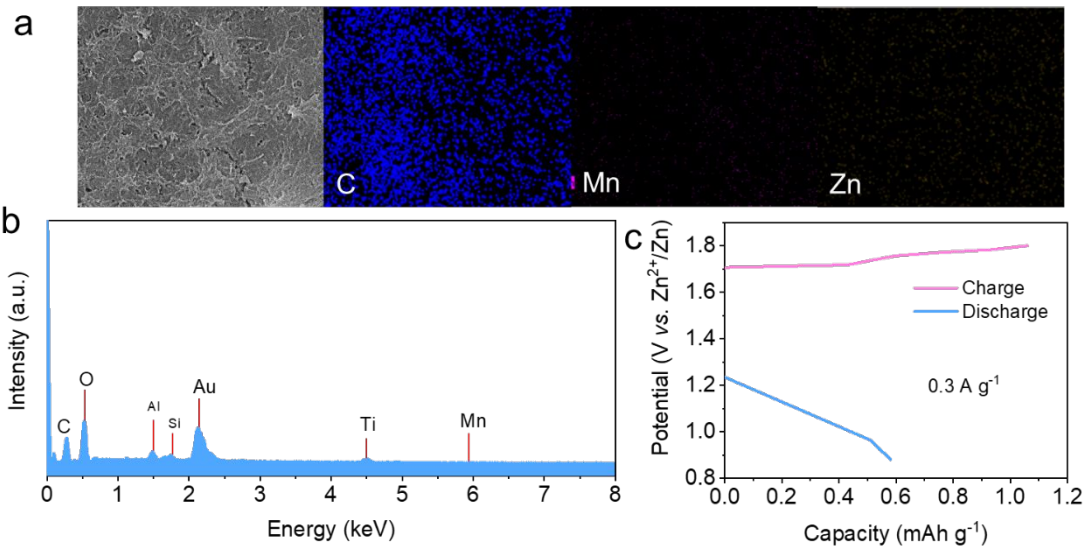

Figure S7. a) the EDS mapping, b) EDS curve of pure conductive carbon black electrode after first charging process, and c) the GCD curves of conductive carbon black electrode during first cycle. Referring the load of active material about 2 mg cm^{-2}, the load of conductive carbon black is about 0.7 mg cm^{-2}.

The charged capacity of carbon electrode is much lower than the first charging capacity of $Ca_2Mn_3O_8$. Therefore, the negligible deposition of Mn demonstrate that the decreased ratio of Ca and Mn is mainly ascribed to Ca^{2+} extraction, rather than Mn deposition.

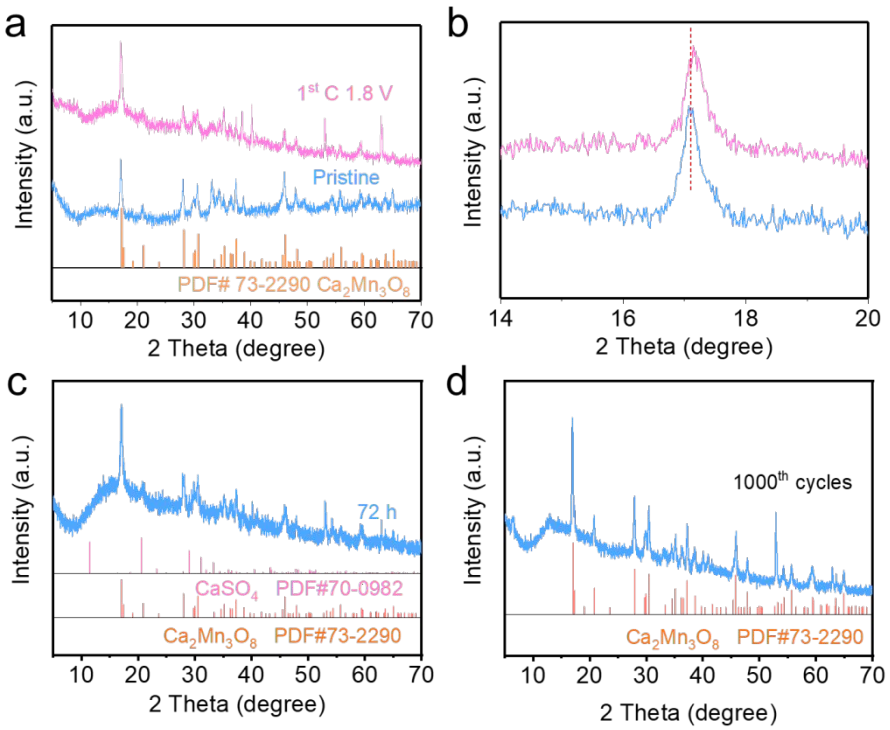

Figure S8. The XRD pattern of a), b) different electrodes at the pristine and 1st charge, c) the soaked electrode in the 3M $ZnSO_4$ with 0.3M $MnSO_4$ electrolyte after 72h, and d) the electrode after 1000 cycles.

As shown in Figure S8a and S8d, the crystal structure maintain stability without obvious structural deformations or phase transition during cycling.

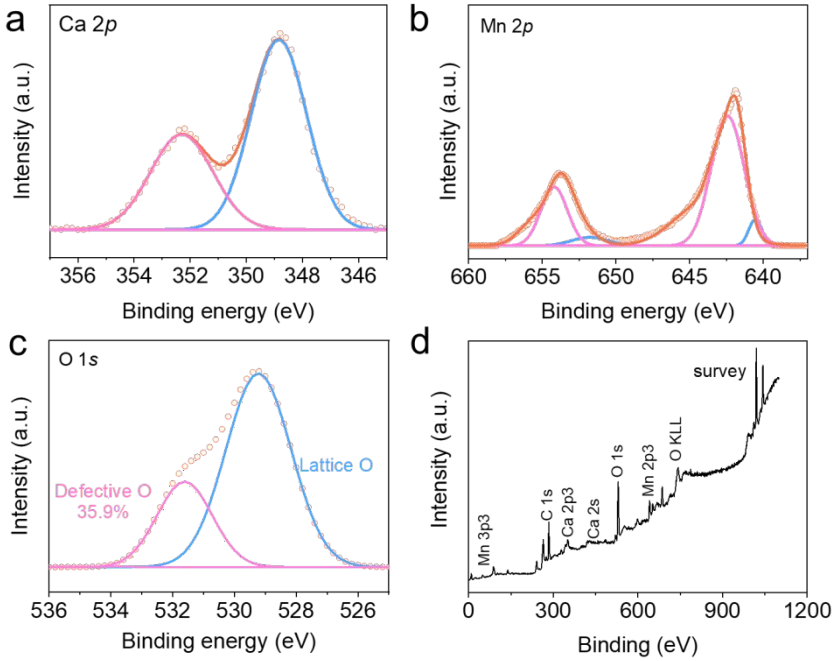

Figure S9. The high-resolution a) Ca 2p, b) Mn 2p, c) O 1s XPS spectra, and d) XPS survey spectra of full charged electrode.

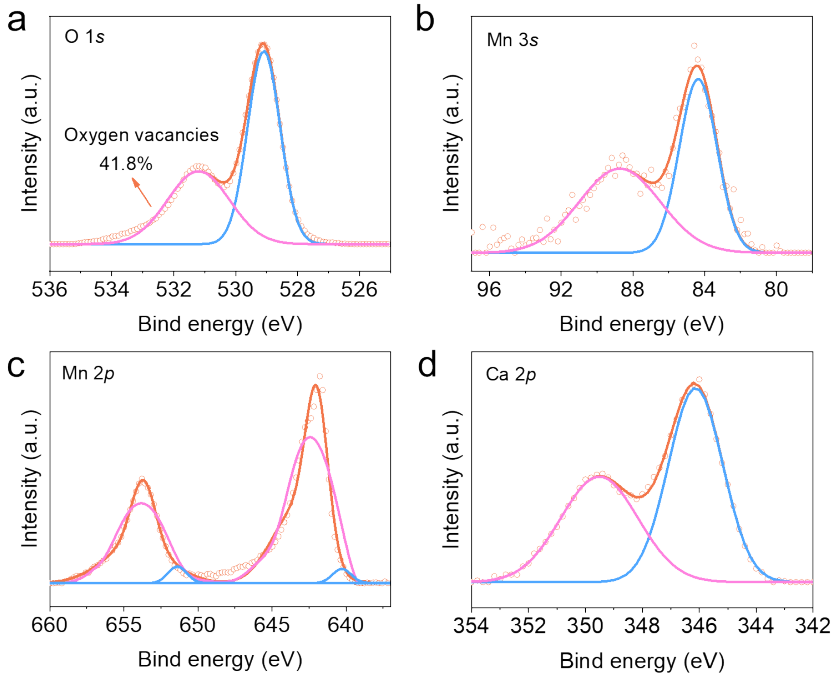

Figure S10. The XPS spectra of a) O 1s, b) Mn 3s, c) Mn 2p and d) Ca 2p after etching 8 nm.

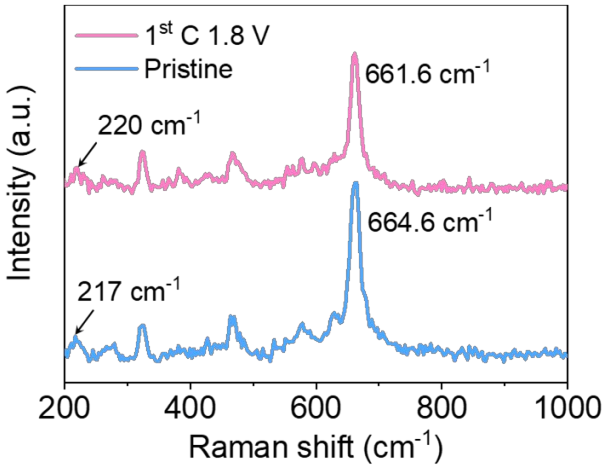

Figure S11. The Raman spectrums of different electrodes at the pristine and 1st charge.

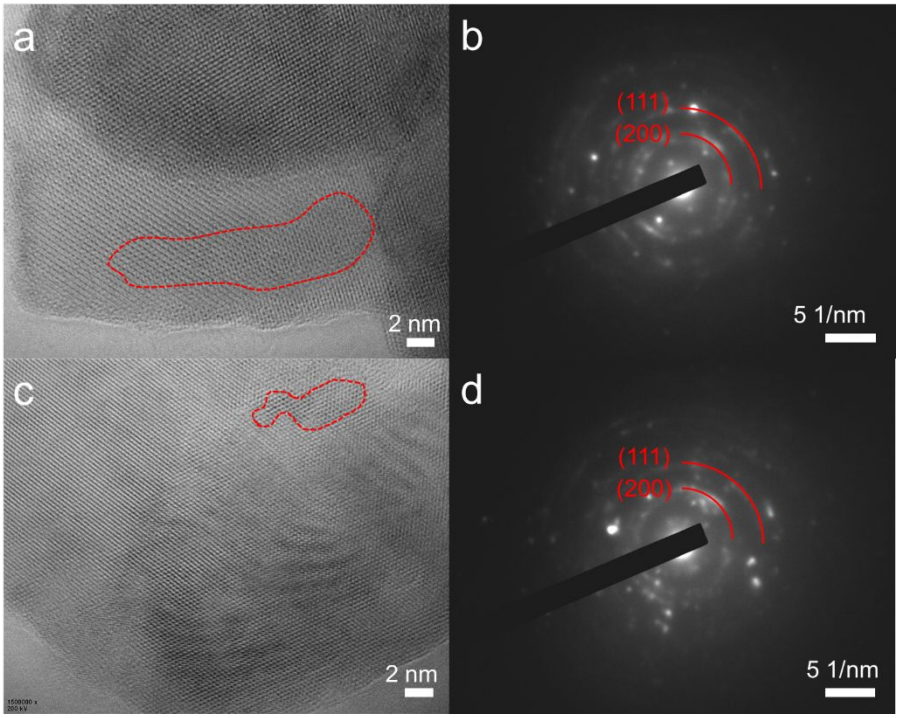

Figure S12. The HRTEM images and corresponding SAED of cathode after a), b) first charged and c), d) fifth charged cycles.

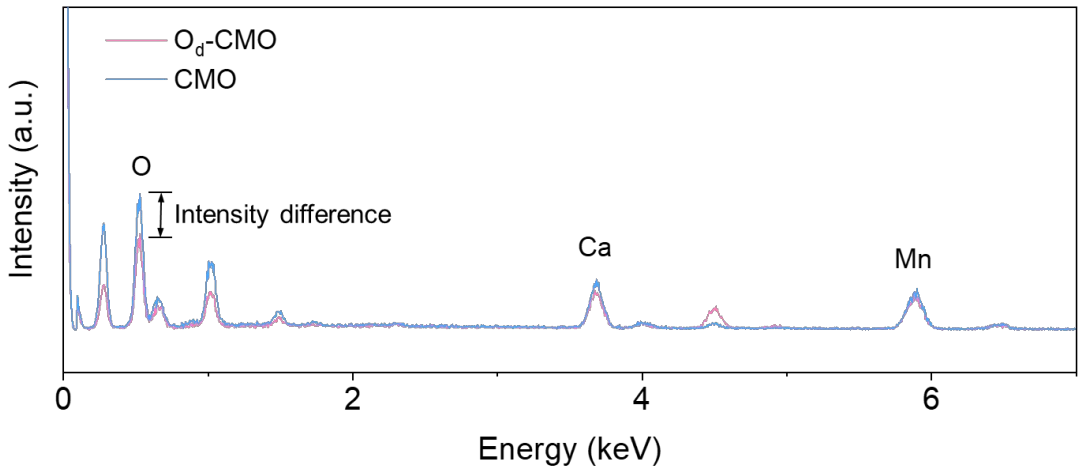

Figure S13. The EDX curves of CMO and O_d-CMO.

The content of Ca and O decrease after charged process, and the S and Zn come from the residuum of $Zn(CF_3SO_3)_2$ electrolyte. Normalizing the Mn signal intensity, Figure S13 shows that the oxygen concentration in the oxygen-vacancies electrode is lower than that the pristine electrode, indicating ~ 3.1% oxygen loss at the outmost surface layer.

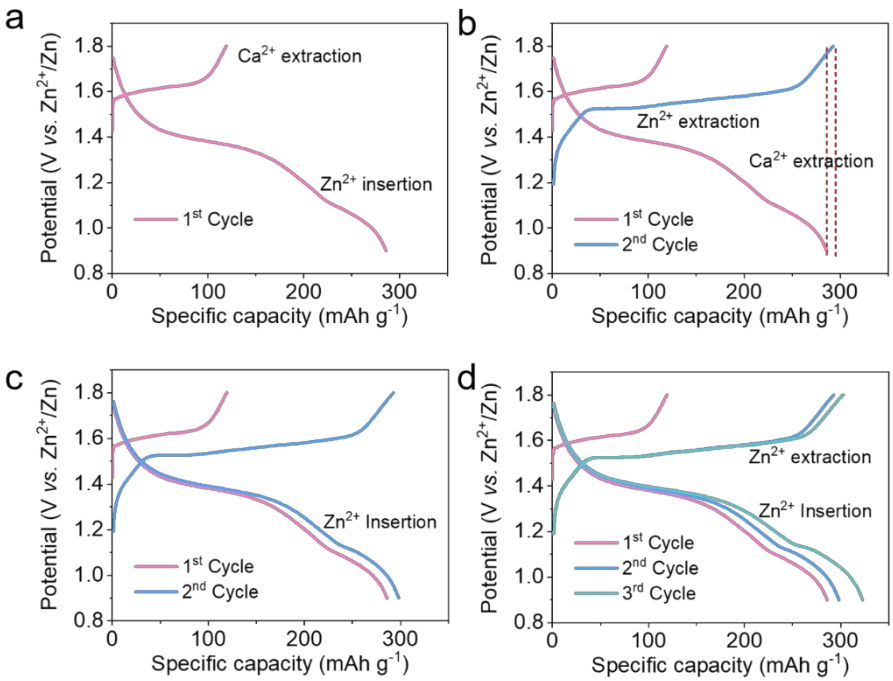

Figure S14. (a-d) The GCD curves of $Ca_2Mn_3O_8$ during cycling.

In fact, the oxygen vacancies formation is strongly related to the activation process. In the initial charging process, the Ca^{2+} is extracted from the manganese oxide layer. To eliminate the charge imbalance caused by calcium deintercalation, oxygens escape from its crystal lattice, leading to the formation of oxygen vacancies in the material.[9] During the discharging process, due to the radius and the inserted energy barrier of Ca^{2+} larger than that of Zn^{2+}, the ions of insertion layers is the Zn^{2+} rather than Ca^{2+} (Figure S12a). Furthermore, during the second cycle, the charged capacity is higher than the first discharged capacity, indicating less Ca^{2+} extraction out (Figure S12b). Owing to the increase oxygen vacancies, more Zn^{2+} are inserted, and the discharge capacity also increases (Figure S12c). Similarly, the same process happens in the third cycle. With the decreased concentration of Ca in the bulk phase, the interaction between Ca^{2+} and MnO_6 octahedron is strengthened, and the difficulty of Ca^{2+} extraction is increased, so the concentration of Ca^{2+} tends to progressively more stable. In conclusion, the formation of the oxygen vacancies and the activation process are strongly associated with the process of Ca^{2+} extraction.[10]

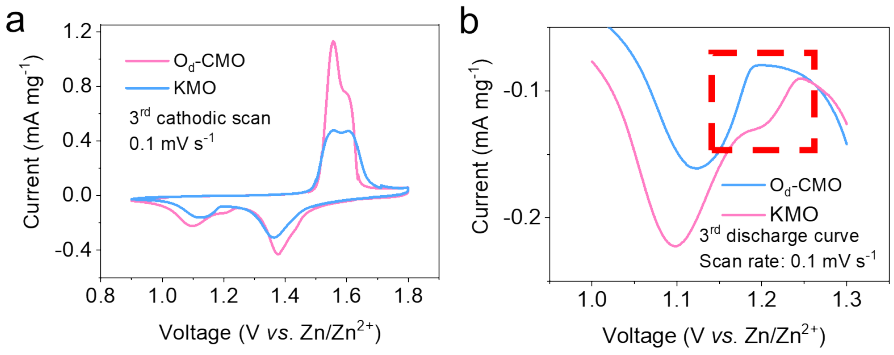

Figure S15. a) the CV curves at 0.1 mV s^{-1} of the third cycle for the O_d-CMO and KMO electrodes, and b) detailed image

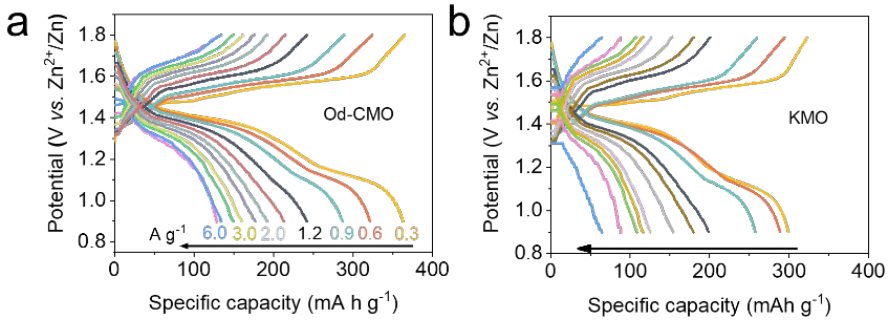

Figure S16. Galvanostatic charge/discharge curves at different current densities of a) O_d-CMO and b) KMO.

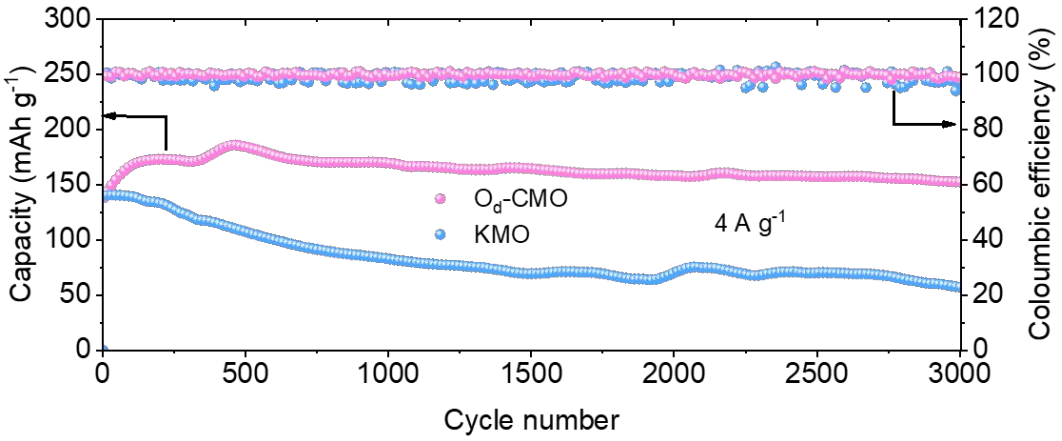

Figure S17. The prolonged cycling performance of O_d-CMO and KMO at 4 A g^{-1}.

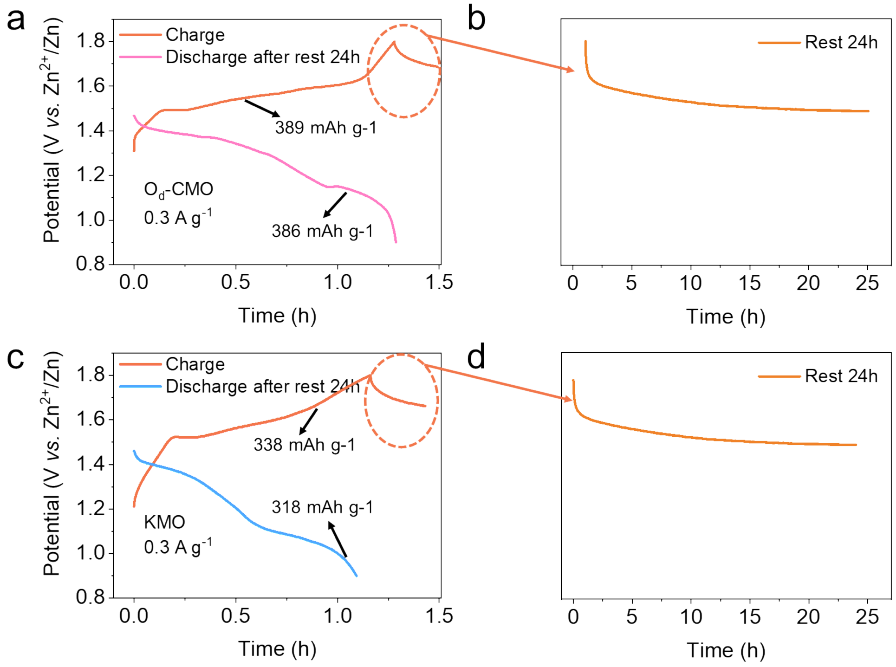

Figure S18. Self-discharge behavior tested at a current density of 0.3 A g^{-1}, a), b) the O_d-CMO and c), d) the KMO when firstly charged to 1.8 V, and discharged to 0.9 V after rest for 24 hours.

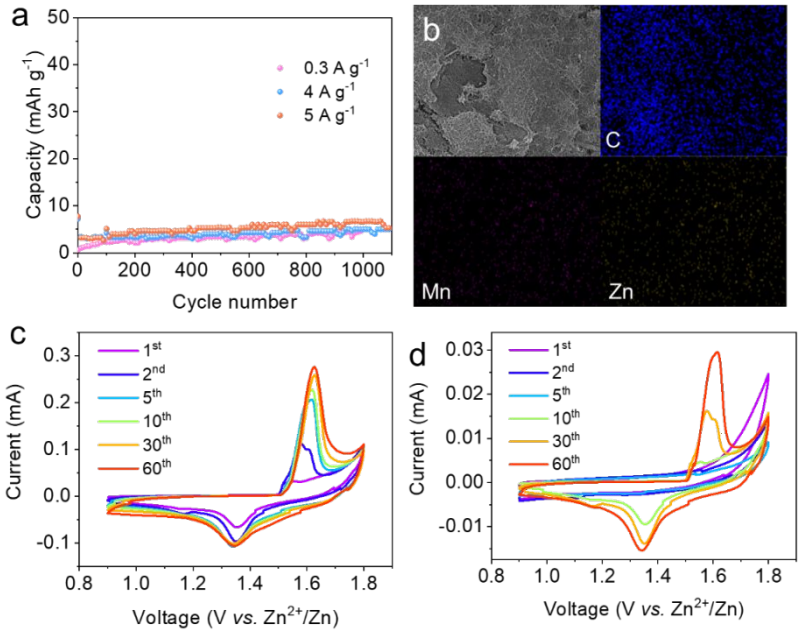

Figure 19. a) the long cycle of conductive carbon black electrode at the current density of 0.3 A g^{-1},4 A g^{-1} and 5 A g^{-1}, b) the EDS mapping of fully charged conductive carbon black electrode after 1000 cycles under the current density of 5 A g^{-1}, the CV curves of carbon black electrode in the c) 3M $ZnSO_4$ with 0.3M $MnSO_4$ and d) 3M $Zn(CF_3SO_3)_2$ with 0.3M $Mn(CF_3SO_3)_2$ electrolyte.

After 1000 cycles, the low capacity and unobvious EDS mapping of Mn proved the limited deposition of Mn (Figure S19). In the 3M $ZnSO_4$ and 0.3M $MnSO_4$ solution, the oxidation peaks of 1.5-1.7 V and reduction peaks of 1.2-1.4 V became more and more obvious during cycling, indicating the deposition and dissolution of Mn. However, in the 3M $Zn(CF_3SO_3)_2$ and 0.3M $Mn(CF_3SO_3)_2$ solution, the peak current of redox peak was 0.03 mA, which much smaller than 0.3 mA in the 3M $ZnSO_4$ and 0.3M $MnSO_4$ solution, suggesting that the unobvious deposition of Mn. Above phenomenon confirm the results that the dissolution and deposition of manganese was not the main energy storage mechanism for O_d-CMO.

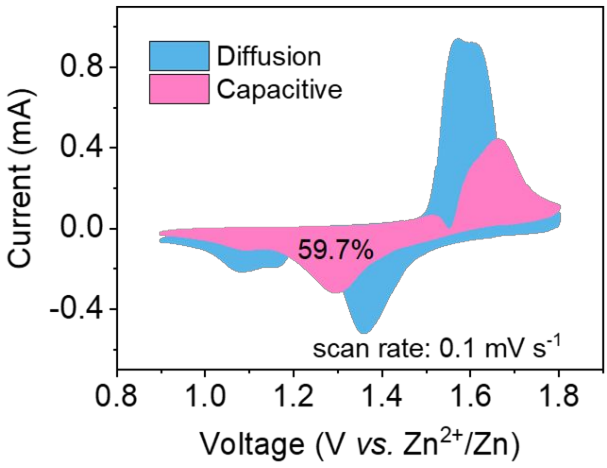

Figure S20. The pseudocapacitive contribution of O_d-CMO at 0.1 mV s^{-1}.

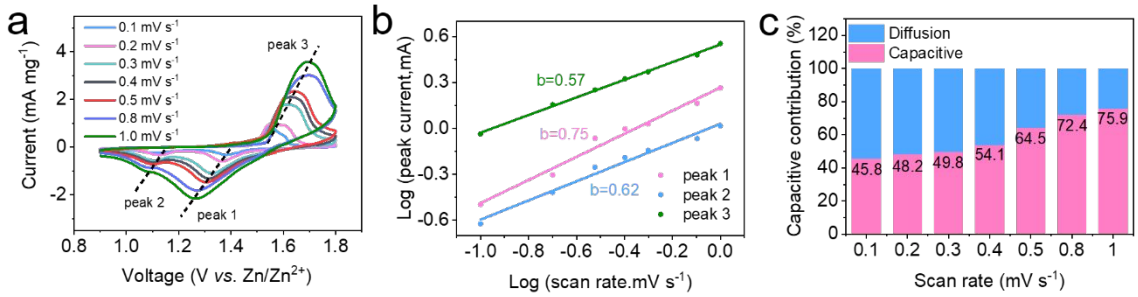

Figure S21. a) the CV curves at a different scan rate of KMO, b) the relationship between Logarithmic pattern of current and scan rate at specific peaks, c) the proportion of capacitive and diffusion contributions at a different scan rate.

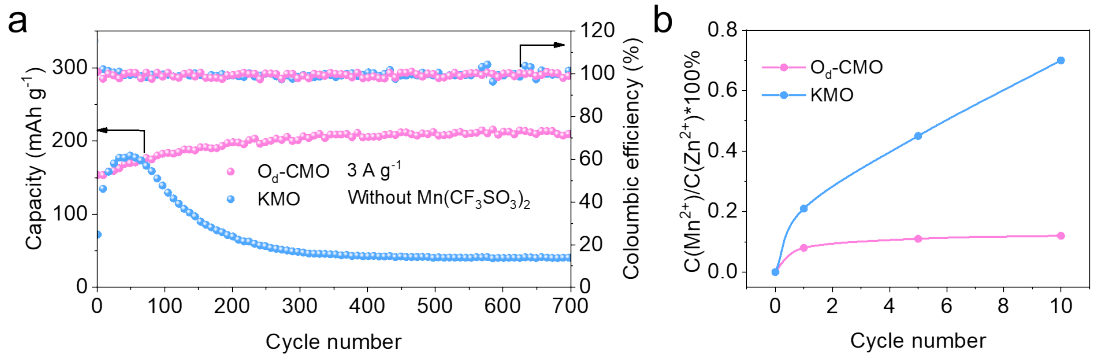

Figure S22. a) comparison of cycle performance and coulombic efficiency in the 3M $Zn(CF_3SO_3)_2$ without $Mn(CF_3SO_3)_2$, b) comparison of manganese dissolution rate of O_d-CMO and KMO in different cycles.

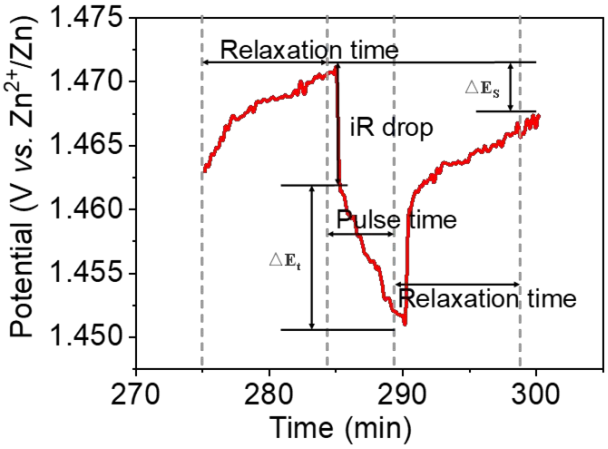

Figure S23. E *vs.* t curves of $Ca_{1.65}Mn_3O_{7.2}$ electrode for a single GITT during the discharge process.

The Galvanostatic Intermittent Titration Technique (GITT) is usually used to estimate the solid diffusion coefficient according to the following equation:[11]

$$D^{\mathrm{GITT}}=\frac{4}{\pi\tau}\left(\frac{m_B V_M}{M_B S}\right)^2\left(\frac{\Delta Es}{\Delta E_\tau}\right)^2$$

Where τ is the duration of the relaxation (s); t is the duration of current pulse; m_B is the quality of the active material (g); the V_M is the molar volume ($cm^3\ mol^{-1}$); the M_B is the molar mass of the electrode material ($g\ mol^{-1}$); the S is the total contacting area of

electrode with electrolyte (cm^2); the ΔE_S is the steady-state potential change (V) by the current pulse; and ΔE_τ is the potential change (V) during the constant current pulse after eliminating the iR drop.

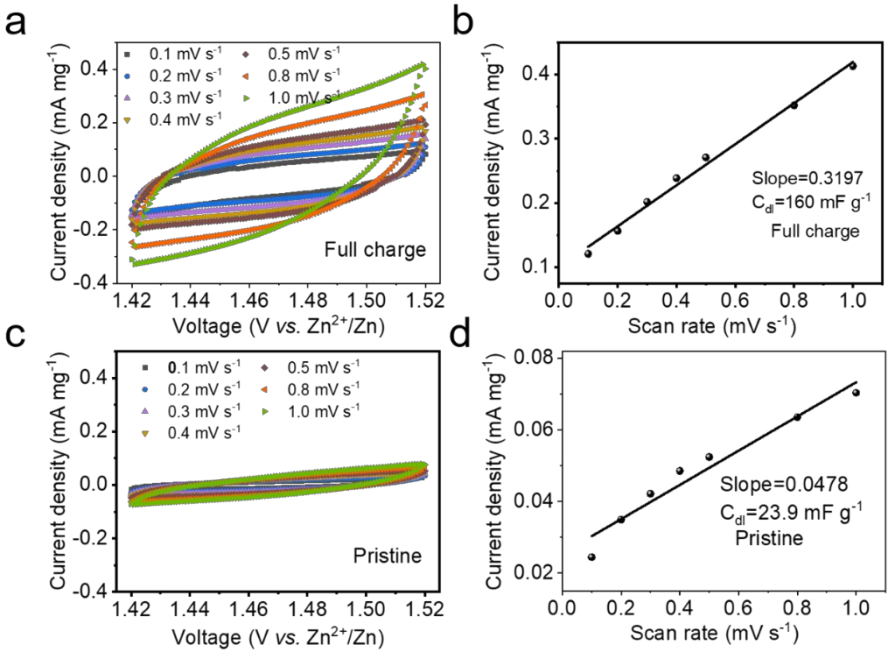

Figure S24. CV curves and linear fit of current densities versus scan rates of a), b) oxygen-vacancies O_d-CMO and c), d) pristine $Ca_2Mn_3O_8$. The electrochemical active surface area (ECSA) was estimated by electrochemical double-layer capacitance (C_{dl}).[3,12]

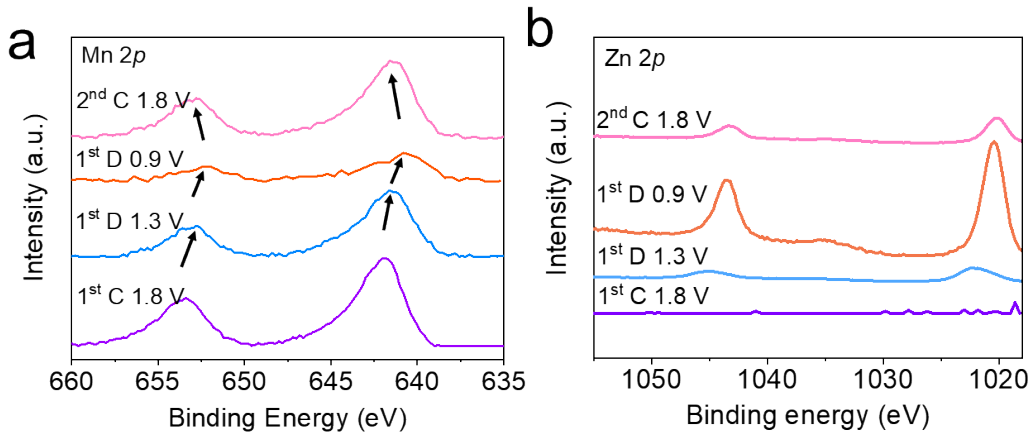

Figure S25. The ex-situ a) Mn 2p and b) Zn 2p high-resolution XPS spectrum of O_d-CMO electrode at different status.

Table S1. The ICP-OES analysis of $Ca_2Mn_3O_8$ and electrolyte at different states.

Sample	C_{Ca}/mg L^{-1}	C_{Mn}/mg L^{-1}	C_{Ca}/C_{Mn}
Initial	121.5	261.2	0.6611
1st charge to 1.8 V	23.36	59.89	0.5543
1st discharge to 0.9 V	20.26	51.77	0.5562
2nd charge to 1.8 V	27.79	49.77	0.5584
3rd charge to 1.8 V	23.68	62.14	0.5392
5th charge to 1.8 V	21.71	58.16	0.5305
1st charged electrolyte	1.02	185.6	$7.531*10^{-3}$

Table S2. Summary of the electrochemical performance comparison of various defective manganese-based oxides batteries.

Cathode materials	**Average discharging voltage [V]**	**Capacity [mAh g^{-1}]**	**Energy density [Wh kg^{-1}]**	**Power density [kW kg^{-1}]**	**Cycle stability**	**Reference**
oxygen-deficient δ-MnO_2	1.36	345	470	10	≈80% after 2000 cycles at 5 A g^{-1}	[4]
oxygen-deficient β-MnO_2	1.32	302	400	≈1.5	≈94% after 500 cycles at 0.5 A g^{-1}	[8]
oxygen-deficient $ZnMn_2O_4$	1.24	221	273.4	2.6	≈45% after 300 cycles at 1.66 A g^{-1}	[7]
oxygen-deficient $K_{0.8}Mn_{0.8}O_{16}$	1.32	302	≈400	≈3	≈75% after 1000 cycles at 1 A g^{-1}	[13]
Mn vacancy ε-MnO_2	-	570	409	-	≈92% after 1800 cycles at 30 mA cm^{-2}	[14]
Mn-deficient MnO	1.19	300	356	2.7	≈99% after 1500 cycles at 1A g^{-1}	[15]
cation-defective $ZnMn_2O_4$	1.35	150	202	-	≈94% after 500 cycles at 0.5 A g^{-1}	[16]
Oxygen-vacancies $Ca_2Mn_3O_8$	**1.39**	**368**	**512**	**7.5**	**≈92% after 3000 cycles at 5 A g^{-1}**	**This work**

Table S3. The fitted results of electrolyte resistance R_S and charge-transfer resistance R_{ct} of $Ca_2Mn_3O_8$ and MnO_2.

Sample		Rct/Ω	Rs/Ω
O_d-CMO	Initial	351	0.708
	1st cycle	75.5	0.436
	10th cycle	56.7	0.516
	50th cycle	53.3	0.0156
KMO	Initial	170	0.663
	1st cycle	324	0.653
	10th cycle	359	0.634
	50th cycle	649	3.34

Reference:

(1) Sun, T.; Nian, Q.; Zheng, S.; Shi, J.; Tao, Z. Layered $Ca_{0.28}$ $MnO_2 \cdot 0.5H_2O$ as a High Performance Cathode for Aqueous Zinc-Ion Battery. *Small* **2020**, *2000597*, 1–8.

(2) Yabuuchi, N.; Kajiyama, M.; Iwatate, J.; Nishikawa, H.; Hitomi, S.; Okuyama, R.; Usui, R.; Yamada, Y.; Komaba, S. P2-Type $Na_x[Fe_{1/2}$ $Mn_{1/2}]O_2$ Made from Earth-Abundant Elements for Rechargeable NaÂ Batteries. *Nat. Mater.* **2012**, *11* (6), 512–517.

(3) Xia, C.; Jiang, Q.; Zhao, C.; Hedhili, M. N.; Alshareef, H. N. Selenide-Based Electrocatalysts and Scaffolds for Water Oxidation Applications. *Adv. Mater.* **2016**, *28* (1), 77–85.

(4) Xiong, T.; Yu, Z. G.; Wu, H.; Du, Y.; Xie, Q.; Chen, J.; Zhang, Y. W.; Pennycook, S. J.; Lee, W. S. V.; Xue, J. Defect Engineering of Oxygen-Deficient Manganese Oxide to Achieve High-Performing Aqueous Zinc Ion Battery. *Adv. Energy Mater.* **2019**, *9* (14).

(5) Zhang, M.; Wu, W.; Luo, J.; Zhang, H.; Liu, J.; Liu, X.; Yang, Y.; Lu, X.; Lu, X. A High-Energy-Density Aqueous Zinc-Manganese Battery with a La-Ca Co-Doped ϵ-MnO_2 cathode. *J. Mater. Chem. A* **2020**, *8* (23), 11642–11648.

(6) Ramírez, A.; Bogdanoff, P.; Friedrich, D.; Fiechter, S. Synthesis of $Ca_2Mn_3O_8$ Films and Their Electrochemical Studies for the Oxygen Evolution Reaction (OER) of Water. *Nano Energy* **2011**, *1* (2), 282–289.

(7) Zhang, H.; Wang, J.; Liu, Q.; He, W.; Lai, Z.; Zhang, X.; Yu, M.; Tong, Y.; Lu, X. Extracting Oxygen Anions from $ZnMn_2O_4$: Robust Cathode for Flexible All-Solid-State Zn-Ion Batteries. *Energy Storage Mater.* **2019**, *21*, 154–161.

(8) Han, M.; Huang, J.; Liang, S.; Shan, L.; Xie, X.; Yi, Z.; Wang, Y.; Guo, S.; Zhou, J. Oxygen Defects in β-MnO_2 Enabling High-Performance Rechargeable Aqueous Zinc/Manganese Dioxide Battery. *iScience* **2020**, *23* (1).

(9) Hou, J.; Li, Y.; Mao, M.; Zhao, X.; Yue, Y. The Effect of Ce Ion Substituted

OMS-2 Nanostructure in Catalytic Activity for Benzene Oxidation. *Nanoscale* **2014**, *6* (24), 15048–15058.

(10) Guo, S.; Liang, S.; Zhang, B.; Fang, G.; Ma, D.; Zhou, J. Cathode Interfacial Layer Formation via in Situ Electrochemically Charging in Aqueous Zinc-Ion Battery. *ACS Nano* **2019**, *13* (11), 13456–13464.

(11) Li, W.; Corradini, D.; Body, M.; Legein, C.; Salanne, M.; Ma, J.; Chapman, K. W.; Chupas, P. J.; Rollet, A. L.; Julien, C.; Zhagib, K.; Duttine, M.; Demourgues, A.; Groult, H.; Dambournet, D. GITT-High Substitution Rate in TiO_2 Anatase Nanoparticles with Cationic Vacancies for Fast Lithium Storage. *Chem. Mater.* **2015**, *27* (14), 5014–5019.

(12) Ji, H.; Zhao, X.; Qiao, Z.; Jung, J.; Zhu, Y.; Lu, Y.; Zhang, L. L.; MacDonald, A. H.; Ruoff, R. S. Capacitance of Carbon-Based Electrical Double-Layer Capacitors. *Nat. Commun.* **2014**, *5*, 3317-3323.

(13) Fang, G.; Zhu, C.; Chen, M.; Zhou, J.; Tang, B.; Cao, X.; Zheng, X.; Pan, A.; Liang, S. Suppressing Manganese Dissolution in Potassium Manganate with Rich Oxygen Defects Engaged High-Energy-Density and Durable Aqueous Zinc-Ion Battery. *Adv. Funct. Mater.* **2019**, *29* (15), 1–9.

(14) Chao, D.; Zhou, W.; Ye, C.; Zhang, Q.; Chen, Y.; Gu, L.; Davey, K.; Qiao, S. Z. An Electrolytic Zn-MnO_2 Battery Demonstrated for High-Voltage and Scalable Energy Storage. *Angew. Chemie - Int. Ed.* **2019**, *58* (23), 7823–7828.

(15) Zhu, C.; Fang, G.; Liang, S.; Chen, Z.; Wang, Z.; Ma, J.; Wang, H.; Tang, B.; Zheng, X.; Zhou, J. Electrochemically Induced Cationic Defect in MnO Intercalation Cathode for Aqueous Zinc-Ion Battery. *Energy Storage Mater.* **2019**, *24* (April), 394–401.

(16) Zhang, N.; Cheng, F.; Liu, Y.; Zhao, Q.; Lei, K.; Chen, C.; Liu, X.; Chen, J. Cation-Deficient Spinel $ZnMn_2O_4$ Cathode in $Zn(CF_3SO_3)_2$ Electrolyte for Rechargeable Aqueous Zn-Ion Battery. *J. Am. Chem. Soc.* **2016**, *138* (39), 12894–12901.